Quantitative Detection of Myoglobin Content in Tan Mutton During Cold Storage by Near-infrared Hyperspectral Imaging

Yourui Sun[1] · Haonan Zhang[2] · Guishan Liu[1] · Jianguo He[1] · Lijuan Cheng[1] · Yue Li[1] · Fangning Pu[2] · Hao Wang[2]

Abstract

The discolorations or abnormal colors in meat and meat products during processing and storage have negative effects on their commercial value. In this study, myoglobin content (MetMb and OxyMb) in Tan mutton was rapidly detected using near-infrared hyperspectral imaging (NIR-HSI) system (900–1700 nm), and built predictive models with full wavebands (FW) based on partial least squares regression (PLSR), least-squares support vector machines (LSSVM), and back propagation neuron network (BP). To reduce the computational complexity of calibration models, feature bands were obtained by bootstrapping soft shrinkage (BOSS), variable combination population analysis coupled with iteratively retains informative variables (VCPA-IRIV), and competitive adaptive reweighted sampling (CARS), respectively. The optimized BP model based on feature wavebands with BOSS method selection displayed the best capability for predicting MetMb level ($R^2_C = 0.8340$, $R^2_P = 0.8253$ $RMSEC = 3.1592$, $RMSEP = 3.2918$). In addition, the simplified VCPA-IRIV-BP model was significant in predicting OxyMb content with R^2_C, R^2_P, $RMSEC$, and $RMSEP$ values of 0.8024, 0.8680, 3.4676, and 2.7605, respectively. Results provided a theoretical reference for rapid evaluation of myoglobin content in other animal products via NIR-HSI.

Keywords Tan mutton · Quantitative detection · Near-infrared hyperspectral imaging · Myoglobin content · Variable selection · Back propagation neuron network

Introduction

Besides its commercial value, mutton is a wealth source of protein, vitamins, and minerals (Yu et al. 2021a). Tan sheep, an important local sheep breed in Ningxia, China, is famous for its high-quality mutton. With the improvement of consumers' awareness of food safety, there is a high demand for the quality of meat products. As a traditional meat-preservation method, low-temperature storage delays

the deterioration of meat and thus prolongs shelf life and maintains meat quality (Coombs et al. 2017). Although activities of the microorganism can be restrained by low temperature during cold storage, some reactions, such as psychrophilic microbial activity and enzymatic hydrolysis reaction, are still active (Cheng et al. 2021), which directly lead to the discoloration of Tan mutton in the process of processing, transportation, and sales. Meat color usually influences consumers' appetites for merchandise; the discoloration or abnormal color in meat and meat products during shelf life has negative effects on their commercial value (Maria and Luis. 2014; Mancini and Hunt 2005; Mancini and Ramanathan 2020).

Meat color is closely related to the relative content of three different chemical forms of myoglobin: deoxymyoglobin (DeoMb, amaranth), oxygenated myoglobin (OxyMb, bright red), and metmyoglobin (MetMb, grayish brown), respectively (Mancini and Hunt 2005; Nguyen et al. 2016, 2019). In general, DeoMb predominates in meat before slaughter (Shin et al. 2021). As meat is exposed to air after slaughter, the DeoMb on the meat surface is quickly transformed into OxyMb in the oxygenation process. Besides,

Yourui Sun and Haonan Zhang contributed equally.

✉ Guishan Liu
Liugs@nxu.edu.cn

Yourui Sun
youruisun@163.com

Haonan Zhang
zhanghn_2020@163.com

[1] School of Food & Wine, Ningxia University, Yinchuan 750021, China

[2] School of Physics and Electronic-Electrical Engineering, Ningxia University, Yinchuan 750021, China
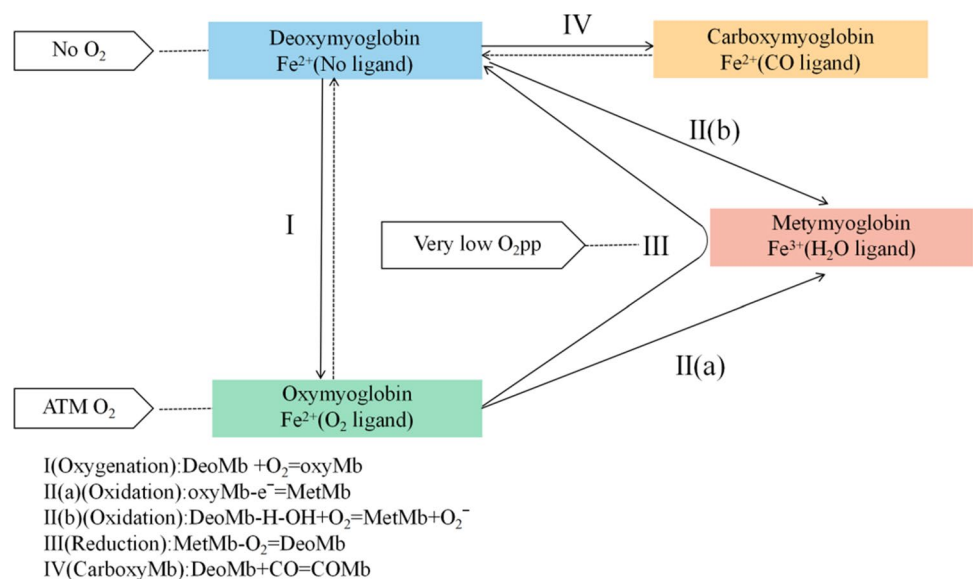
oxidation occurs from the interior of the meat, which transforms DeoMb and OxyMb into MetMb (Nguyen et al. 2016). Meanwhile, the contents of MetMb and OxyMb have dominant position after slaughter. The myoglobin redox state for the surface of postmortem muscle is shown in Fig. 1.

Traditional analytical methods for assessing myoglobin in meat include sensory evaluation and chemical determination (Mancini 2013). However, the disadvantages of these methods are that they require cumbersome pre-processing, complicated operation, copious consumption of reagents, destructive detection for samples, and so forth, failing to meet the rapid, accurate, and nondestructive requirements of modern food industry. Moreover, the different levels of experiment proficiency may cause errors in measurement (Kuswandi and Nurfawaidi 2017; Shin et al. 2021). In recent years, hyperspectral imaging (HSI) technology has been widely applied in agricultural product detection because of its fast and non-destructive characteristics, and has become promising in evaluating and monitoring food quality (Ma and Sun 2020). HSI could simultaneously acquire spectral and spatial information at each pixel of an object. Spectral images are three-dimensional (3-D) in nature, with two spatial dimensions and one spectral dimension [hypercubes (x, y, λ)] (Qin 2013). The most important application of HSI in meat is line-scanning, which is significant for fundamental food research owing to its high resolutions and rapid scanning speed (Ma et al. 2019). Recently, HSI has been utilized to measure the parameters related to the internal and external qualities of meat, such as pH (Barbin et al. 2012), fat content (Lohumi et al. 2016), thiobarbituric acid reactive substances (TBARS) (Cheng et al. 2019), meat tenderness (Knight et al. 2019), total volatile basic-nitrogen (TVB-N) (Baek et al., 2021), bacterial food-borne pathogens (Bonah et al. 2020), and fatty acid (Wang et al. 2020a). The detection of meat

color by using hyperspectral imaging was mainly focused on L*, a*, and b* values (ElMasry et al. 2012; Jiang et al. 2018; Kamruzzaman et al. 2016; Wu et al. 2012). Regarding the content of myoglobin, Yuan et al. (2020) and Cheng et al. (2021) found that Vis/NIR and NIR hyperspectral imaging could be employed to detect myoglobin. Wan et al. (2020) used the HSI (900–1700 nm) for a non-destructive detection of the contents of DeoMb, OxyMb, and MetMb in nitrite-cured mutton during refrigerated storage. It could be inferred from these studies that although hyperspectral imaging has shown the potential for myoglobin prediction, the predictability of MetMb content by Yuan et al. (2020) was obtained with $R^2_P = 0.7654$ and $RMSEP = 2.9306$, the model performances are still inadequate and much improvement is required. It could also be drawn from the studies mentioned above that this modality needs to further develop robust algorithms for the analysis of aberrations from desirable characteristics and improving computational strategies of predictive model before application to meat products. For instance, Wan et al. (2020) found that a total of 36 and 33 feature wavelengths for OxyMb and MetMb were selected by CARS, respectively. Nevertheless, it is still necessary to reduce the dimensionality of band and improve the band selection performance by BOSS and VCPA-IRIV algorithm.

Therefore, the aims of the current study were to (a) evaluate the effectiveness of different pre-processing methods and select the optimal method; (b) perform BOSS, VCPA-IRIV, and CARS as reference technologies to identify and extract key wavebands that were closely related to the myoglobin of Tan mutton to simplify predictive models; and (c) analyze and optimize quantitative strategies (such as PLSR, LSSVM, and BP) to predict the content of myoglobin (MetMb and OxyMb) based on key wavebands and full wavebands. Figure 2 presents the schematic description of

Fig. 1 Myoglobin redox state for the surface of postmortem muscle

I(Oxygenation):DeoMb +O₂=oxyMb
II(a)(Oxidation):oxyMb-e⁻=MetMb
II(b)(Oxidation):DeoMb-H-OH+O₂=MetMb+O₂⁻
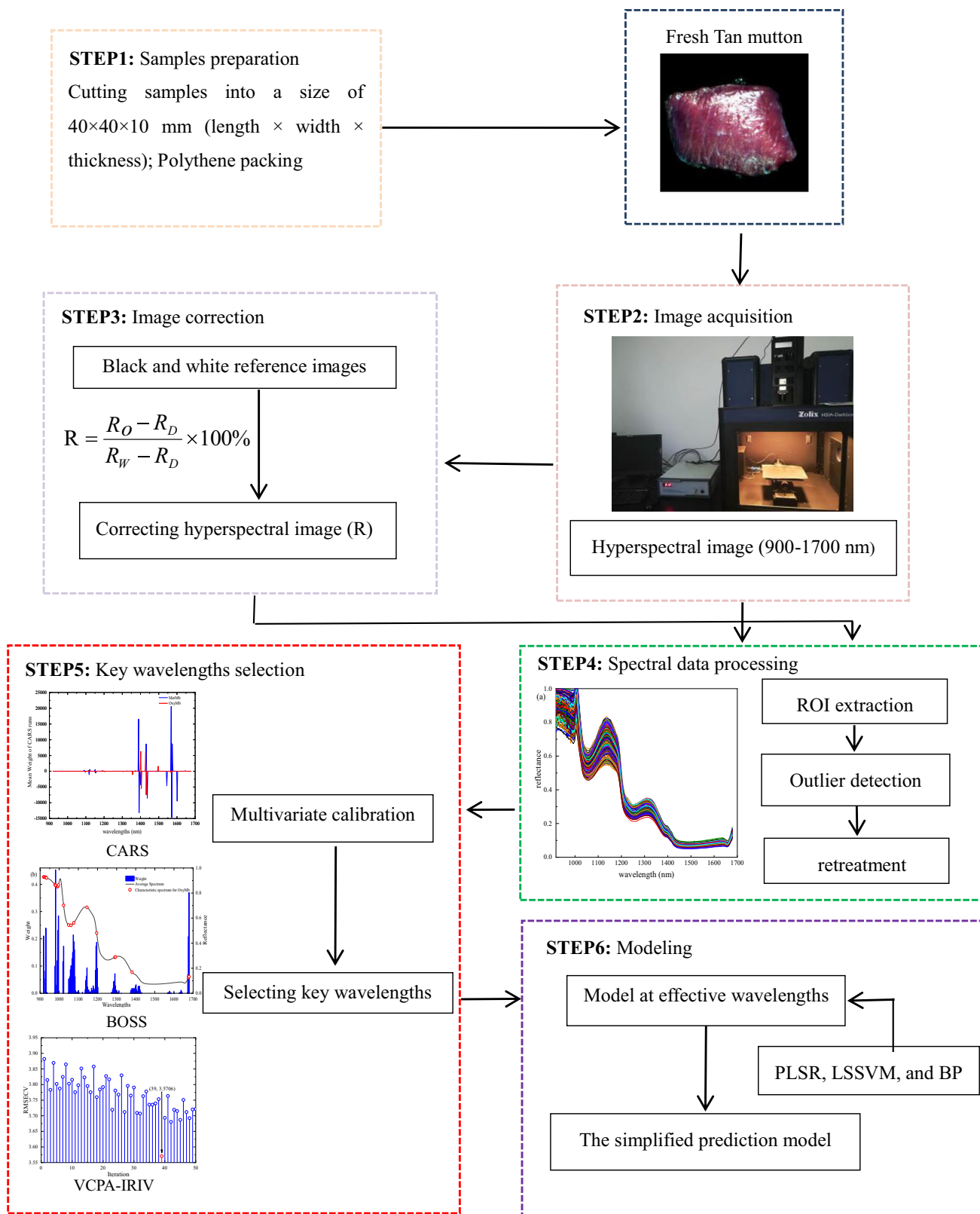III(Reduction):MetMb-O₂=DeoMb
IV(CarboxyMb):DeoMb+CO=COMb

Fig. 2 The schematic description of the HSI method depicting the whole experimental processes

the HSI detection method toward myoglobin content of Tan mutton during cold storage.

Materials and Methods

Sample Preparation

The experiment was conducted in the laboratory of agricultural products non-destructive testing, School of Food & Wine, Ningxia University. Samples from the longissimus dorsi of Tan sheep were purchased from a local marketplace in Ningxia, China. All these carcasses were individually placed in a portable refrigerated incubator covered with ice, which was similar to the storage conditions of the refrigerator and then transported to our lab within 2 h and stored at 4℃. After the chilling and aging of the carcasses, samples were removed of fat and connective tissue, and then cut into a size of $40 \times 40 \times 10$ mm; finally, 200 pieces obtained were collected for investigation. All samples were randomly divided into 10 groups, individually packaged by a polythene bag, labeled, and stored in a refrigerator at 4℃. During experiment, each mutton sample was wiped off the surface moisture to obtain its spectral image and then to measure the myoglobin contents during different storage times (1, 4, 7, 10, 13, 16, 19, 22, 25, and 28 days). The spectral and experimental measurements were conducted at a room temperature of 21℃ during winter.

Myoglobin was extracted from Tan mutton by following the method of Krzywicke (1982) with minor modifications. Firstly, 5-g Tan mutton samples were chopped in 25 mL phosphate buffer (0.04 mol/L, pH 6.8), evenly mixed, and then homogenized at 10,000 r/min for 25 s by an ultrafine homogenizer. Secondly, the homogenized solution was stored at 4℃ for 1 h in the dark, centrifuged at 6000 g at 4℃ for 15 min, and the supernatant was filtered. Finally, the absorbance of the filtrate was read at 525, 545, 565, and 572 nm using a UV-2401PC spectrophotometer (Shimadzu Inc., Columbia, MD, USA) with phosphate buffer as blank, respectively. The contents of MetMb and OxyMb were calculated as follows:

$$[MetMb] = (-2.514R_a + 0.777R_b + 0.800R_c + 1.098) \times 100$$

$$\left[OxyMb\right] = (0.882R_a + 1.267R_b + 0.809R_c - 0.361) \times 100$$

Here, R_a, R_b, and R_c were absorbance ratios of $A_{572\,nm}/A_{525\,nm}$, $A_{565\,nm}/A_{525\,nm}$, and $A_{545\,nm}/A_{525\,nm}$, respectively.

Hyperspectral Acquisition

Hyperspectral data was obtained by InGaAs camera (Models XC-130 100 Hz, Ophir Optronics Solutions Ltd., Jerusalem,

Israel) with a spectral range from 900 to 1700 nm and four 35 W halogen lamps (ViP V-light, Lowel Light Inc., NY, HSIA-LS-TDIF, Zolix instruments Co., Ltd., Beijing, China) in a dark box. Each mutton sample was placed on a mobile platform and scanned with a linear array push-scan (ImSpector N17E, Specim, Spectral Imaging Co., Ltd., Oulu, Finland). HSI system was preheated for 30 min before image acquisition (Cheng et al. 2021). The spectral images of samples were collected by SpectraCube software.

To reduce noises and invalid information caused by dark current and uneven illumination in the InGaAs device of HSI system, it was necessary to calibrate with dark (R_D) and white (R_W) references before getting the hyperspectral images (Liu et al., 2019). The bright and dark currents were corrected before measurement. The correction formula was as follows:

$$R = \frac{R_O - R_D}{R_W - R_D} \times 100\%$$

R is the relative spectral reflectance after correction, and R_O, R_D, and R_W are the experimental spectral reflectance, dark current spectral reflectance, and bright current spectral reflectance, respectively (Wu et al., 2013).

Spectral Data Analysis

Pre-processing of Spectral Data

The spectral reflectance of each mutton sample was extracted via ENVI 4.8 software, and the region of interest (ROI) was used to manually operate and extract the average spectrum of the target region.

Original spectral data may be affected by the signal noise from the uneven surface of Tan mutton samples, as well as the baseline drift, scattered light, and other factors during the hyperspectral image collection. Therefore, it is necessary to perform the spectral pre-processing on hyperspectral images for increasing computation speed and improving the stability and robustness of model. In the present study, some pre-processing methods of spectral data including baseline (Yang et al. 2021), normalize (Feng et al., 2019), Gaussian filter (GF) (Yuan et al. 2021), moving average (MA) (Tao and Peng 2015), Savitzky-Golay (SG) (Chen et al. 2011), and combinations thereof were used to improve model prediction performance.

Feature Waveband Selection

Hyperspectral data contain a large amount of information (e.g. spectral bands), causing the analysis to be time-consuming. Additionally, most bands are independent of the final prediction. Therefore, feature waveband selection is a

core procedure to reduce the dimension of calibration data and complexity of calibration model for improving calculation speed (Lorente et al. 2012). In this study, competitive adaptive reweighted sampling (CARS), bootstrapping soft shrinkage (BOSS), and variable combination population analysis coupled with iteratively retaining informative variables (VCPA-IRIV) were employed to select feature wavebands.

BOSS algorithm is used to generate random combination of variables and construct sub-models by combined bootstrap sampling (BBS) and weight bootstrap sampling (WBS) techniques (Jiang et al. 2021). Model population analysis (MPA) is adopted to extract variable information from submodels (Deng et al. 2016). CARS is a variable selection method which simulates the "survival of the fittest" principle of Darwin's evolution theory. The bands with larger absolute value of regression coefficient are selected from partial least squares (PLS) model by adaptive reweighted sampling (ARS) technique in an iterative and competitive manner (Shao et al. 2021). N subsets of variables are screened out through N samplings, and the subset with the lowest *RMSECV* value is referred to optimal feature bands (Wang et al. 2020b). VCPA-IRIV is used to minimize the variable space and maintain a specific number of variables for further computation of IRIV (Yun et al. 2019). IRIV is implemental to optimize the variable space created by VCPA. A mixed-methods approach of VCPA utilizes its advantages in constantly lessening the variable space and retaining significant variables to overcome the disadvantages of IRIV in calculation with a large number of variables (Yu et al. 2021b).

Model Development

In this study, partial least squares regression (PLSR), back propagation neuron network (BP), and least-squares support vector machines (LSSVM) were employed to build quantitative models to predict the myoglobin content in Tan mutton after slaughter.

As a linear multivariate regression method, PLSR has been widely used to construct the relationships among spectral measurements, including correlation variables, chemical composition determination indexes and so on. In this study, the model was utilized to predict the content of myoglobin in Tan mutton. Latent variables (LVs) were extracted, and the calibration model was validated by leave-one-out crossvalidation to avoid overfitting or underfitting and to achieve good performances (Feng et al. 2018a). LSSVM algorithm is an extension of the support vector machine (SVM), which can be used in approximate nonlinear systems with higher accuracy. There are two major parameters that determine the accuracy of model on LSSVM: kernel function parameter (σ^2) and regularization parameter (γ). The generalization

capacity of the model augments with the reduction of the γ, but the training error increases, and the smaller the σ^2, the higher the complexity of the model and the larger the σ^2, which can easily lead to under-learning (Mo et al. 2020). There are three layers in a BP model called the input layer, the hidden layer, and the output layer (Ma et al. 2019). The model is trained by comparing the differences between the network output and the reference property and by minimizing their error with changing the linkage weights (ElMasry et al. 2009). Then, the BP is built with acceptable errors by continuously adjusting the weights.

Model Evaluation

Some statistical parameters including the coefficients of determination in calibration (R^2_C), prediction (R^2_P), full cross-validation (R^2_{CV}), the root mean square errors in calibration (*RMSEC*), prediction (*RMSEP*), and cross-validation (*RMSECV*) (Cascant et al. 2016) were used to evaluate model performance. While R^2 between 0.66 and 0.81 was acceptable, values between 0.82 and 0.90 and above 0.90 represented good and excellent results (Karoui et al. 2006). RMSE was calculated between predictive and observed values (Feng et al. 2018b). Therefore, a good model has low values of *RMSEC* and *RMSEP*, the differences between these two values are extremely small, and high values of R^2c, R^2cv, and R^2p (Feng et al. 2019). The formulas for R^2 and *RMSE* were as follows:

$$R^2 = \frac{\sum\limits_{j=1}^{n}\left(y_j - \bar{y}_j\right)^2 - \sum\limits_{j=1}^{n}\left(y_j - \hat{y}_j\right)^2}{\sum\limits_{j=1}^{n}\left(y_j - \bar{y}_j\right)^2}$$

$$RMSE = \sqrt{\frac{1}{n}\sum\limits_{j=1}^{n}\left(\bar{y}_j - y_j\right)^2}$$

where y_j and $\hat{y}_j$ are the practical measured value and predictive estimated value, respectively; $\bar{y}_j$ is the mean of reference measurement; and n is the number of samples.

Software

PLSR and pre-processing methods were implemented via Unscrambler X10.4 software (Version 10.4, CAMO, Oslo, Norway). The procedures of SPXY, CARS, BOSS, VCPA-IRIV LSSVM, and BP were executed via MATLAB R2019a software (The Mathworks Inc., Natick, MA, USA). Identifications of a region of interest (ROI) and extraction of spectral data were achieved via ENVI 4.8 software (ITT Visual Information Solutions, Boulder, Co., Ltd., USA).

Results and Discussion

NIR Spectral Features of Samples

The original and mean reflectance spectra extracted from Tan mutton samples in the range of 900–1700 nm were depicted in Fig. 3. Figure 3b shows the differences in the reflectance of the curves in the visible region. Samples of reflectance in the range of 910 to 1400 nm differed in the magnitude of reflectance but not in trends. Generally, the peaks were observed in the NIR region of meat components broad bands arising from highly overlapping bands of the chemical bonds C-H, O–H, and N–H groups (Kamruzzaman 2012; Osborne 2000). In the NIR band, the major absorption bands were observed in 1005, 1241, and 1443 nm. The absorption wavelengths near 1200 nm (1241 nm) and 1600–1700 nm were due to C-H stretching the 1st and 2nd overtone, respectively (Wang et al. 2020a), while those near 1400–1660 nm (1443 nm) were due to the 1st overtone of O–H and the 2nd overtone of N–H stretching modes of water-bonded groups (Pu et al. 2015).

Outliers

Samples that affected model performance were examined as abnormal samples. Based on the distributions of means and standard deviation (SD) of prediction errors for MetMb and OxyMb in each sample, Monte Carlo outlier method (Zhang 2017) was used to detect anomalous samples. The outlier values were removed from the original data, and the remaining data were used to build PLSR detection model. The overall performance of model was improved for the detection of MetMb and OxyMb upon the removal of outliers, with the R^2c increased from 0.7993 to 0.8164 and 0.7785 to 0.8183, respectively, and the *RMSECV* decreased from 5.2565 to 4.9425 and 4.4732 to 3.9735, respectively. As shown in Table 1, calibration set and prediction set were divided by SPXY algorithm, and the means and SD for the calibration and prediction set were compared, which signified an analogous sample spread between those two sets. The advantage of SPXY can effectively bestow the multi-dimensional vector space and thus enhance the robustness of the model (Wei et al., 2020).
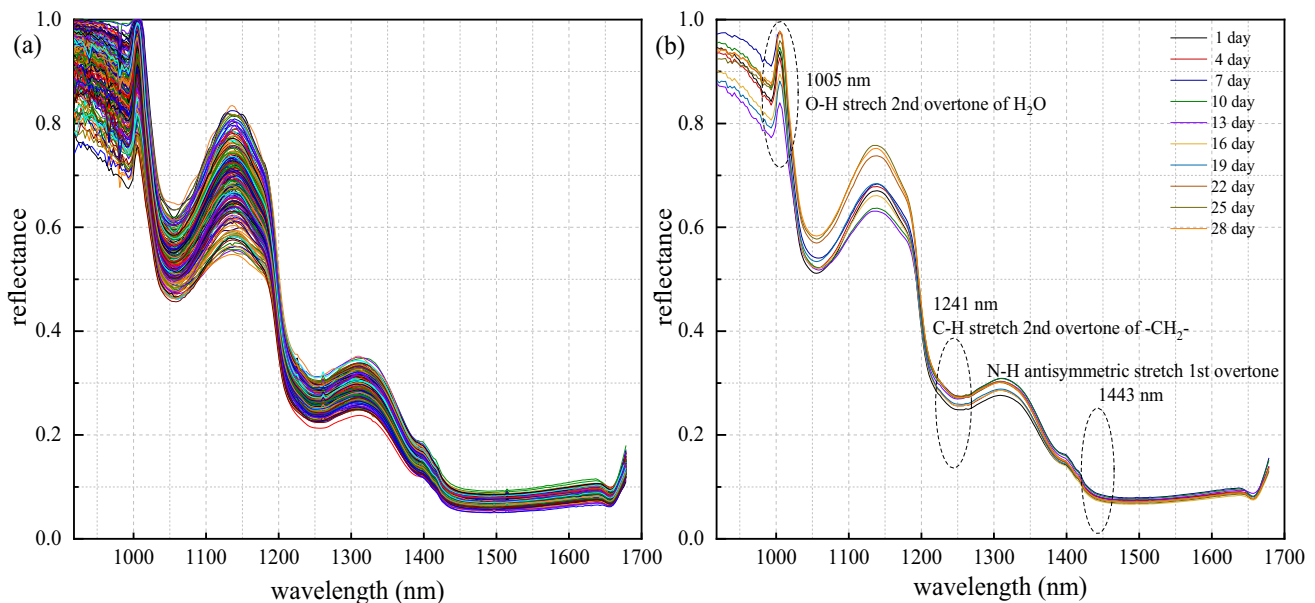

Fig. 3 Spectral curves of samples with different storage periods. **a** Original spectral curves; **b** mean spectral curves

Table 1 Statistics of relative MetMb and OxyMb contents of samples

Subsets	Calibration set						Prediction set					
	N	Max	Min	Mean	SD	CV(%)	N	Max	Min	Mean	SD	CV(%)
MetMb	145	54.0224	16.3248	33.4178	9.5920	28.70	49	50.6423	17.8136	36.5319	9.4420	25.85
OxyMb	142	53.8122	24.0138	38.4713	7.7360	20.11	47	50.6403	24.7749	35.5443	7.5919	21.36

Pre-processing of Spectral Data

The original spectra can be rectified by pre-processing method to enhance the resolution of overlapping data and reduce the instrument drift scattering and system noise. Figure 4 shows the results of performance of full wavelength model with references MetMb and OxyMb values based on different pre-processing methods. MA-SG pre-processing displayed the highest accuracy for prediction. The R^2_p values of the optimal models for the contents of MetMb and OxyMb were 0.7217 and 0.7911, respectively, which were higher than the bound with raw data. And the $R^2_C = 0.8355$, 0.8152, $RMSEC = 3.8906$, 3.3256, and $RMSEP = 5.2304$, 4.3763, respectively. Therefore, the most appropriate pre-processing method of predicting the MetMb and OxyMb contents of the mutton samples was MA-SG. Compared with original spectra, the results were improved by the MA-SG pre-processing, which might be explained by decreased scattering effects or eliminating signal noises. To reduce interference information, MA and SG have been widely used in HSI research (Vaiphasa 2006). Weng (2020) and Tao and Peng (2015) found that SG and MA obtained good results in hyperspectral scattering imaging.

Feature Waveband Selection

After being pre-processed by MA-SG, a total of 256 wavebands for MetMb and OxyMb were obtained in the NIR range (900–1700 nm). To decrease the dimensionality of spectral data and computation time, CARS, VCPA-IRIV, and BOSS were employed to select feature wavebands from the full spectra range. Each variable selection method had randomness in the operation process and influenced the reliability of the prediction model. Each

of the above algorithms was calculated 50 times. Finally, the minimum value of *RMSECV* was selected as the final feature wavelength selection result of each variable selection method. *RMSECV* values reduced with the deletion of irrelevant bands. When *RMSECV* reached its minimal value, the optimal bands were obtained (Shao et al. 2021; Xu et al. 2019).

Figure 5 presents the extraction of feature wavelengths by using CARS algorithm; the CARS weight peaks or valleys for reflectance were mainly in the spectral range from 1050 to 1150 nm or from 1300 to 1670 nm for MetMb (900 to 1250 nm or from 1350 to 1600 nm for OxyMb), indicating that this algorithm could explicate most of the damage information (Fig. 5a). The peaks or valleys of 1050 to 1250 nm were assigned smaller weights than 1350 to 1650 nm, but they still contained some valid information (Fig. 5b), so some effective information of the these bands were extracted. According to the mean weight of every wavelength, 22 and 20 characteristic variables were selected for MetMb and OxyMb (Table 2) accounting for 8.6% and 7.8% of the total wavelengths, respectively. The positions of feature variables are shown in Fig. 5c. Figure 6 depicts the distribution of feature bands selected by BOSS algorithm. WBS is applied to generate the submodel by weight and MPA is used to analyze the submodel to update the weights of features (Deng et al. 2016). The procedure of optimization feature by BOSS, in which less important variables are not eliminated directly but are assigned smaller weights. There were 15 and 21 feature bands for MetMb and OxyMb, respectively, accounting for 5.9% and 8.2% of the total bands. Figure 7 shows the selection of feature wavelengths by using VCPA-IRIV algorithm; Fig. 7 a and c show that when the number of sampling runs was 49 and 39, *RMSECV*
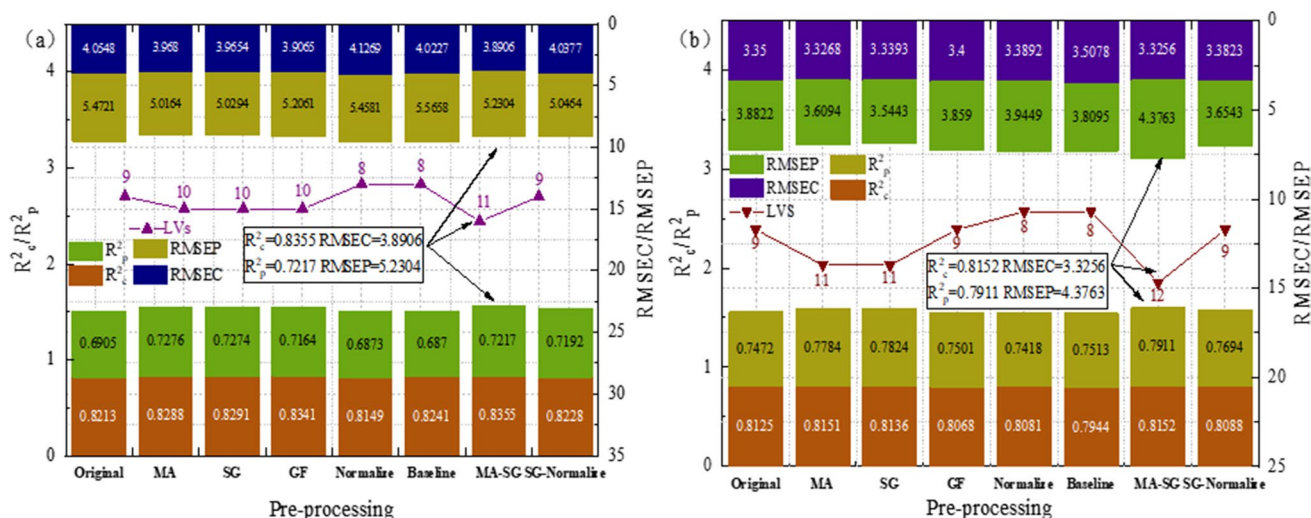

Fig. 4 Performances of full wavelength model based on different pre-processing methods of **a** MetMb and **b** OxyMb
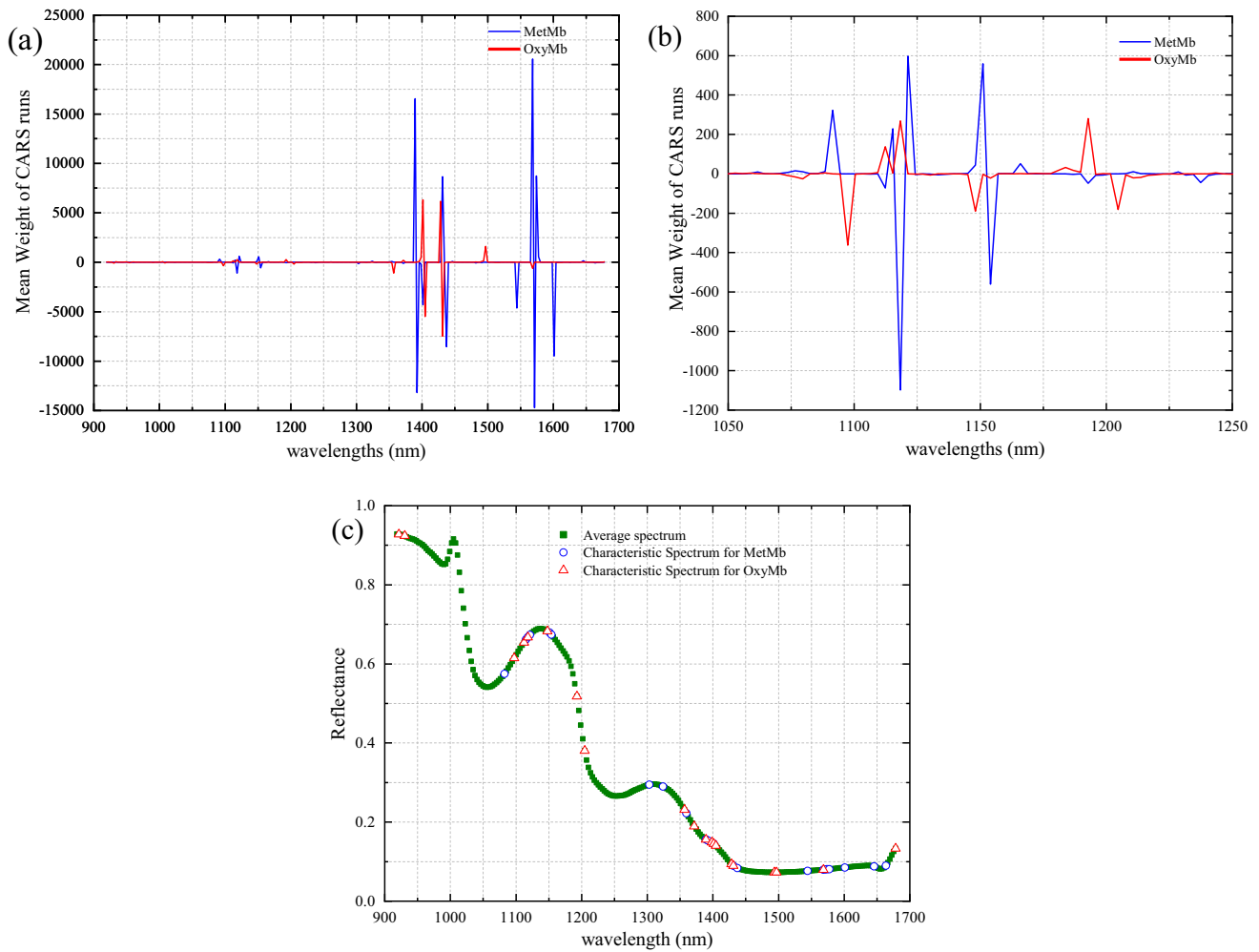
Fig. 5 Running process of selecting optimal variables by CARS algorithm for: mean weight of CARS runs for reflectance (**a** 900–1700 nm; **b** 900–1350 nm); **c** optimal characteristic wavelengths

attained the lowest value of 4.0123 and 3.5706 for MetMb and OxyMb, respectively. As presented in Fig. 7 b and d, a total of 23 and 18 feature wavelengths for MetMb

and OxyMb were selected by VCPA-IRIV from full wavelengths, respectively, accounting for 9.0% and 7.0% of the total wavebands. Those feature wavebands selected

Table 2 Feature waveband selection based on different algorithms

| Category	Methods	Number	Wavelengths (nm)
MetMb	CARS	22	1082, 1115, 1118, 1121, 1151, 1154, 1303, 1323, 1359, 1389, 1392, 1401, 1431, 1437, 1544, 1568, 1571, 1574, 1577, 1601, 1645, 1663
	BOSS	15	981, 996, 1016, 1076, 1079, 1085, 1118, 1136, 1145, 1165, 1195, 1395, 1574, 1642, 1678
	VCPA-IRIV	23	1079, 1085, 1112, 1118, 1142, 1148, 1189, 1192, 1377, 1380, 1386, 1389, 1401, 1425, 1490, 1526, 1538, 1541, 1547, 1562, 1571, 1589, 1642
OxyMb	CARS	20	921, 930, 1097, 1112, 1118, 1148, 1192, 1204, 1356, 1371, 1389, 1398, 1401, 1404, 1428, 1431, 1493, 1496, 1568, 1678
	BOSS	21	918, 921, 927, 930, 933, 978, 981, 990, 993, 996, 1022, 1049, 1061, 1076, 1145, 1195, 1291, 1294, 1380, 1675, 1678
	VCPA-IRIV	18	981, 984, 996, 1040, 1061, 1076, 1118, 1198, 1374, 1398, 1401, 1493, 1496, 1577, 1580, 1672, 1675, 1678
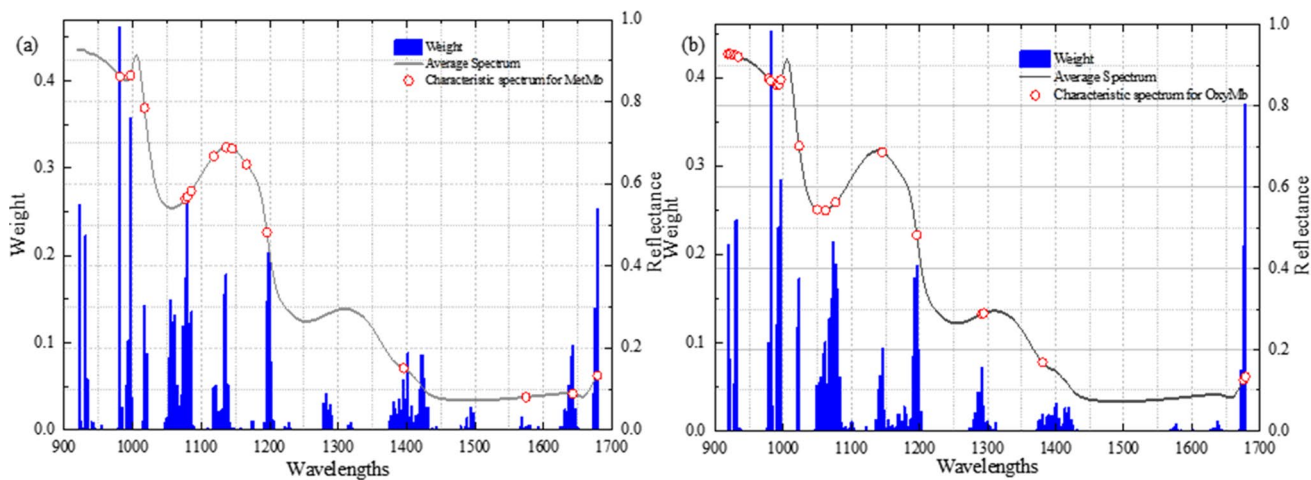
Fig. 6 Running process of selecting optimal variables by BOSS algorithm for MetMb and OxyMb: each feature weight value and optimal characteristic spectrum (**a** for MetMb, **b** for OxyMb)
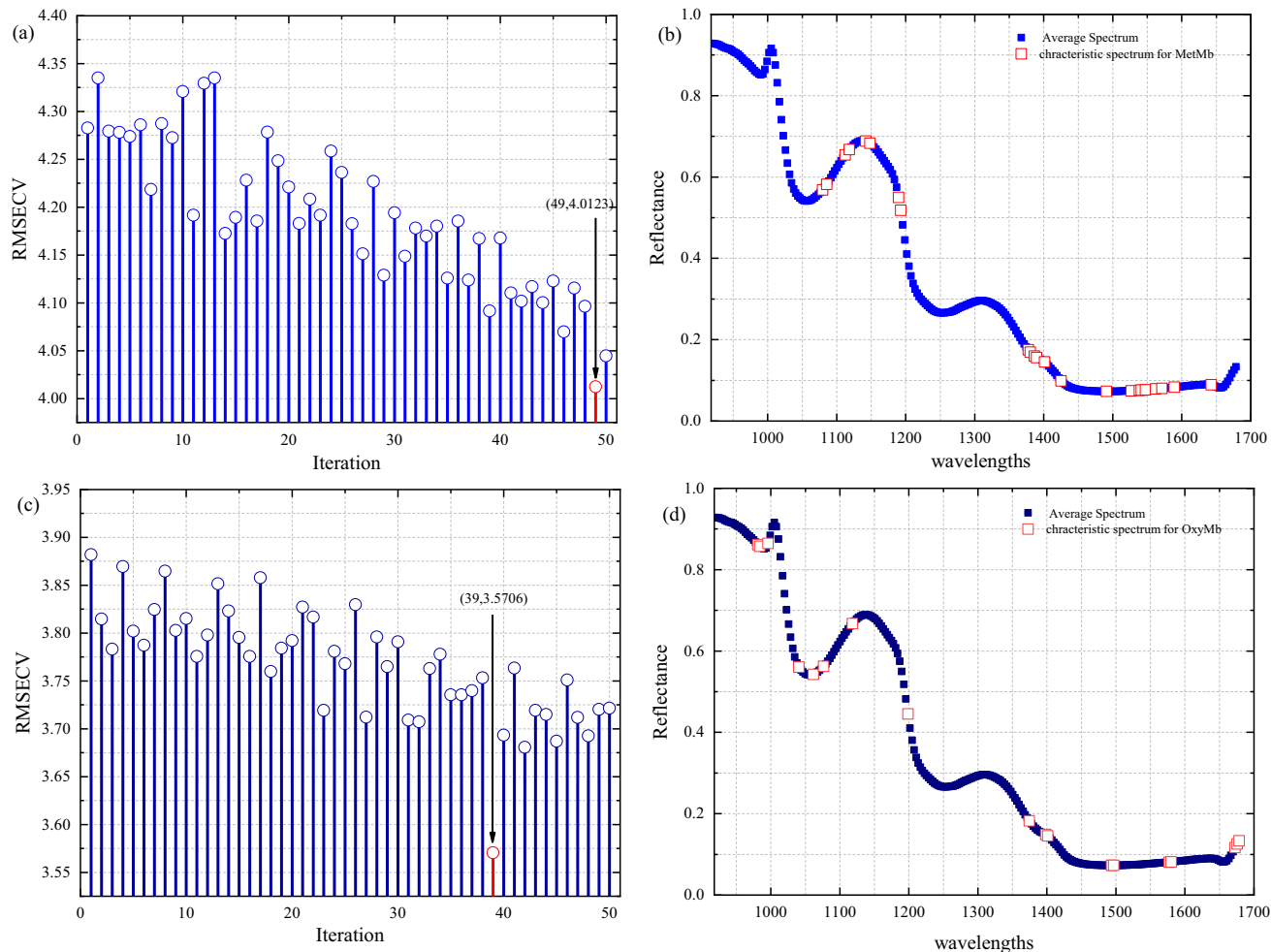

Fig. 7 The variables selected by VCPA-IRIV algorithm for MetMb and OxyMb: **a** the changes in *RMSECV* for MetMb; **b** optimal characteristic wavelengths for MetMb; **c** the changes in *RMSECV* for OxyMb; **d** optimal characteristic wavelengths for OxyMb

by VCPA-IRIV, CARS, and BOSS algorithms are shown in Table 2.

In some cases, the characteristic wavelengths selected in the NIR spectral region were directly related to the molecular bonds of C-H, O–H, and N–H. Absorption bands in the NIR region were observed at 950 nm and at 1456 nm both related to O–H second and first overtones respectively, mainly associated with water content (Barlocco et al. 2006). The extracted effective wavelengths selected in the range of 1100–1400 nm were attributed to combination bands of the C-H stretching and deformation modes (Pu et al. 2015). The key wavelengths selected between 1400 and 1600 nm were related to the first overtones of the O–H and N–H stretching modes of water-bonded groups in meat components (Wan et al. 2020). In addition, feature wavelengths in the 1600–1700 nm were attributed to fat absorption bands related to C-H stretching first overtones (Pu et al. 2015).

Prediction Models Based on Characteristic Wavelengths

In general, PLSR and LSSVM had achieved good results in predicting MetMb and OxyMb contents. As Cheng et al. (2020) found that it was feasible to utilize the prediction model of PLSR, LSSVM in combination with HSI to evaluate the quality of MetMb and OxyMb contents. Compared with PLSR and LSSVM models, BP method was utilized to improve accuracy and robustness of prediction model on the contents of MetMb and OxyMb. The prediction models of MetMb and OxyMb contents were performed by two nonlinear models (BP & LSSVM) and a linear model (PLSR), in which the independent variables of MetMb and OxyMb were predicted from full spectral variables and spectral variables selected by CARS, VCPA-IRIV, and BOSS. The optimal prediction results in PLSR, LSSVM, and BP models for the contents of MetMb and OxyMb in Tan mutton are listed in Table 3. The sequence of model performance was BP > LSSVM > PLSR. As shown in Table 3, BP model based on BOSS emerged the best capability to predict MetMb ($R^2_C = 0.8340$, $R^2_P = 0.8253$ $RMSEC = 3.1592$, $RMSEP = 3.2918$). Besides, the VCPA-IRIV-BP model had a better predictive performance with a higher R^2_C and R^2_P of 0.8024, 0.8680 and a lower $RMSEC$ and $RMSEP$ of 3.4676 and 2.7605 for OxyMb, respectively. It is worth mentioning that CARS algorithms showed a good performance in predicting the contents of MetMb and OxyMb for the selection of feature wavebands. Nevertheless, the number of key wavebands extracted by BOSS and VCPA-IRIV algorithm

Table 3 Performances of feature-wavelength models for predicting contents of MetMb and OxyMb

Category	No. of variables	Model	LVs	Calibration set		Prediction set	
				R^2c	RMSEC	R^2p	RMSEP
MetMb	256	FW-PLSR	11	0.8355	3.8906	0.7217	5.2304
	22	CARS-PLSR	17	0.8586	3.6074	0.7240	5.3394
	23	VCPA-IRIV-PLSR	13	0.8594	3.5966	0.7591	5.0348
	15	BOSS-PLSR	17	0.8358	3.8867	0.7079	5.2945
	256	FW-LSSVM	/	0.8621	3.5686	0.7315	5.0245
	22	CARS-LSSVM	/	0.8947	3.1144	0.7230	5.1800
	23	VCPA-IRIV-LSSVM	/	0.8896	3.1892	0.7642	4.8577
	15	BOSS-LSSVM	/	0.8631	3.5600	0.7033	5.2140
	256	FW-BP	/	0.8415	3.8451	0.7503	4.8801
	22	CARS-BP	/	0.8687	3.4805	0.7502	4.7857
	23	VCPA-IRIV-BP	/	0.8386	3.8738	0.7697	4.5535
	15	**BOSS-BP**	**/**	**0.8340**	**3.1592**	**0.8253**	**3.2918**
OxyMb	256	FW-PLSR	12	0.8152	3.3256	0.7911	4.3763
	20	CARS-PLSR	15	0.8267	3.2204	0.7943	3.5383
	18	VCPA-IRIV-PLSR	9	0.8041	3.4237	0.7808	3.6093
	21	BOSS-PLSR	7	0.8066	3.4023	0.7607	3.7781
	256	FW-LSSVM	/	0.8216	3.2712	0.7915	3.5315
	20	CARS-LSSVM	/	0.8606	2.8910	0.8029	4.4269
	18	VCPA-IRIV-LSSVM	/	0.8118	3.3592	0.8058	3.4324
	21	BOSS-LSSVM	/	0.8220	3.2744	0.7851	3.6245
	256	FW-BP	/	0.7811	3.6281	0.8206	3.4194
	20	CARS-BP	/	0.7665	3.8855	0.8425	3.1071
	18	**VCPA-IRIV-BP**	**/**	**0.8024**	**3.4676**	**0.8680**	**2.7605**
	21	BOSS-BP	/	0.8408	3.8475	0.7403	4.8607

Bold entries indicating the best method and corresponding model performance

was relatively low for the contents of MetMb and OxyMb, respectively. Compared with corresponding full wavelengths models, the simplified VCPA-IRIV-BP and BOSS-BP models indicated better predictive accuracy and robustness. Therefore, BP model was more effective in predicting the MetMb and OxyMb contents in Tan mutton during cold storage than PLSR and LSSVM models. Thus, the potential of NIR-HSI for a quantitative detection of myoglobin content of mutton was identified in this study.

The predictability of MetMb content obtained in this study was higher than that obtained by Yuan et al. (2020) targeting at cooked Tan mutton with $R^2_P = 0.7654$ and $RMSEP = 2.9306$. However, the performances of the OxyMb and MetMb prediction models developed were inferior to that obtained by Cheng et al. (2020) focusing on Tan mutton with $R^2_P = 0.914$ and 0.915 for OxyMb and MetMb, respectively. In addition, Wan et al. (2020) found that the optimal models for OxyMb and MetMb were CARS-PLSR ($Rp = 0.9661$ and $RMSEP = 2.3762$), and CARS-LSSVM ($Rp = 0.8931$ and $RMSEP = 3.2743$) by NIR-HSI system (700–1700 nm), respectively. Those differences related to myoglobin prediction might be explained by different spectral ranges, data processing methods, sample preparations, and packaging methods. Despite the limitation on spectral data processing, this study is encouraging to further investigate the processing methods of hyperspectral images data. The minima of effective information are available to improve model efficiency.

Conclusions

In this study, the NIR-HSI system (900–1700 nm) was adopted to evaluate the MetMb and OxyMb of Tan mutton during cold storage. PLSR, LSSVM, and BP models depended on variable wavelengths which produced superior performances in evaluating MetMb and OxyMb. In contrast, BP model was more appropriate for predicting the contents of MetMb and OxyMb in Tan mutton. CARS, VCPA-IRIV, and BOSS were adopted to extract the optimal wavebands from FW to simplify calibration models. The number of selected characteristic variables was 15 and 23 in BOSS and VCPA-IRIV for MetMb and OxyMb, respectively. As a result, the optimized BP models from characteristic wavelengths were selected by BOSS and VCPA-IRIV for predicting MetMb and OxyMb and exhibited better results than other variable selection methods. The simplified BOSS-BP model yielded good results in assessing MetMb content (R^2_C vs. $R^2_P = 0.8340$ vs. 0.8253, $RMSEC$ vs. $RMSEP = 3.1592$ vs. 3.2918), and the best predictive VCPA-IRIV-BP model showed a better performance with R^2_C, R^2_P, $RMSEC$, and $RMSEP$ values of 0.8024, 0.8680, 3.4676, and 2.7605 for OxyMb. As an emerging and sound technique, HSI can rapidly and non-destructively monitor the safety and quality of mutton. However, some influential factors such as sample types, packaging methods, and storage methods may impact experimental results. Future research might be conducted to augment sample type from different packaging and storage methods by using HSI. Furthermore, analysis methods of spectral data in this study still have a gap compared with classic methods, and it is significant to further explore the spectral data processing and modeling methods to improve data analytical efficiency in future.

Declarations

Ethics Approval This article does not contain any studies with human or animal subjects.

Consent to Participate Not applicable.

Conflict of Interest Yourui Sun declares that she has no conflict of interest. Haonan Zhang declares that he has no conflict of interest. Guishan Liu declares that she has no conflict of interest. Jianguo He declares that he has no conflict of interest. Lijuan Cheng declares that he has no conflict of interest. Yue Li declares that she has no conflict of interest. Fangning Pu declares that he has no conflict of interest. Hao Wang declares that he has no conflict of interest.

References

Barbin DF, Elmasry G, Sun DW, Allen P (2012) Predicting quality and sensory attributes of pork using near-infrared hyperspectral imaging. Anal Chim Acta 719:30–42. https://doi.org/10.1016/j.aca.2012.01.004

Baek I, Lee H, Cho BK, Mo C, Chan DE, Kim MS (2021) Short-wave infrared hyperspectral imaging system coupled with multi-variable method for TVB-N measurement in pork. Food Control 124:107854. https://doi.org/10.1016/j.foodcont.2020.107854

Bonah E, Huang XY, Aheto JH, Yi Y, Yu SS, Tu HY (2020) Comparison of variable selection algorithms on vis-NIR hyperspectral imaging spectra for quantitative monitoring and visualization of bacterial foodborne pathogens in fresh pork muscles. Infrared Phys Technol 107:103327. https://doi.org/10.1016/j.infrared.2020.103327

Barlocco N, Vadell A, Ballesteros F, Galietta G, Cozzolino D (2006) Predicting intramuscular fat, moisture and Warner-Bratzler shear force in pork muscle using near infrared reflectance spectroscopy. Anim Sci 82(01):111–116. https://doi.org/10.1079/ASC20055

Coombs CEO, Holman BWB, Friend MA, Hopkins DL (2017) Long-term red meat preservation using chilled and frozen storage combinations: a review. Meat Sci 125:84–94. https://doi.org/10.1016/j.meatsci.2016.11.025

Cheng LJ, Liu GS, He JG, Wan GL, Ban JJ, Yuan RR, Fan NY (2021) Development of a novel quantitative function between spectral value and metmyoglobin content in Tan mutton. Food Chem 342:128351. https://doi.org/10.1016/j.foodchem.2020.128351

Cheng WW, Sørensen KM, Engelsen SB, Sun DW, Pu HB (2019) Lipid oxidation degree of pork meat during frozen storage investigated by near-infrared hyperspectral imaging: effect of ice crystal growth and distribution. J Food Eng 263:311–319. https://doi.org/10.1016/j.jfoodeng.2019.07.013

Chen HZ, Pan T, Chen JM, Lu QP (2011) Waveband selection for NIR spectroscopy analysis of soil organic matter based on SG smoothing and MWPLS methods. Chemom Intell Lab Syst 107(1):139–146. https://doi.org/10.1016/j.chemolab.2011.02.008

Cascant MM, Sisouane M, Tahiri S, El Krati M, Cervera ML, Garrigues S, Guardia MDL (2016) Determination of total phenolic compounds in compost by infrared spectroscopy. Talanta 153:360–436. https://doi.org/10.1016/j.talanta.2016.03.020

Cheng LJ, Liu GS, He JG, Wan GL, Ma C, Ban JJ, Ma LM (2020) Nondestructive assessment of the myoglobin content of Tan sheep using hyperspectral imaging. Meat Sci 167:107988. https://doi.org/10.1016/j.meatsci.2019.107988

Deng BC, Yun YH, Cao DS, Yin YL, Wang WT, Lu HM, Luo QY, Liang YZ (2016) A bootstrapping soft shrinkage approach for variable selection in chemical modeling. Anal Chim Acta 908:63–74. https://doi.org/10.1016/j.aca.2016.01.001

ElMasry G, Sun DW, Allen P (2012) Near-infrared hyperspectral imaging for predicting colour, pH and tenderness of fresh beef. J Food Eng 110(1):127–140. https://doi.org/10.1016/j.jfoodeng.2011.11.028

ElMasry G, Wang N, Vigneault C (2009) Detecting chilling injury in Red Delicious apple using hyperspectral imaging and neural networks. Postharvest Biology Technology 52(1):1–8. https://doi.org/10.1016/j.postharvbio.2008.11.008

Feng CH, Makino Y (2020) Colour analysis in sausages stuffed in modified casings with different storage days using hyperspectral imaging-A feasibility study. Food Control 111:107047. https://doi.org/10.1016/j.foodcont.2019.107047

Feng XP, Yu CL, Shu ZY, Liu XD, Yan W, Zheng QS, Sheng KC, He Y (2018) Rapid and non-destructive measurement of biofuel pellet quality indices based on two-dimensional near infrared spectroscopic imaging. Fuel 228:197–205. https://doi.org/10.1016/j.fuel.2018.04.149

Feng CH, Makino YOS, Juan FGM (2018) Hyperspectral imaging and multispectral imaging as the novel techniques for detecting defects in raw and processed meat products: Current state-of-the-art research advances. Food Control 84:165–176. https://doi.org/10.1016/j.foodcont.2017.07.013

Feng L, Zhang M, Adhikari B, Guo ZM (2019) Nondestructive detection of postharvest quality of cherry tomatoes using a portable NIR spectrometer and chemometric algorithms. Food Anal Methods 12(4):914–925. https://doi.org/10.1007/s12161-018-01429-9

Jiang HZ, Yoon SC, Zhuang H, Wang W, Li YF, Lu CJ, Li J (2018) Non-destructive assessment of final color and pH attributes of broiler breast fillets using visible and near-infrared hyperspectral imaging: a preliminary study. Infrared Phys Technol 92:309–317. https://doi.org/10.1016/j.infrared.2018.06.025

Jiang H, He YC, Xu WD, Chen QS (2021) Quantitative detection of acid value during edible oil storage by Raman spectroscopy: comparison of the optimization effects of BOSS and VCPA algorithms on the characteristic raman spectra of edible oils. Food Anal Methods. https://doi.org/10.1007/s12161-020-01939-5

Kuswandi B, Nurfawaidi A (2017) On-package dual sensors label based on pH indicators for real-time monitoring of beef freshness. Food Control 82:91–100. https://doi.org/10.1016/j.foodcont.2017.06.028

Knight MI, Linden N, Ponnampalam EN, Kerr MG, Brown WG, Hopkins WL, Baud S, Ball AJ, Borggaard C, Wesley I (2019) Development of VISNIR predictive regression models for ultimate pH, meat tenderness (shear force) and intramuscular fat content of Australian lamb. Meat Sci 155:102–108. https://doi.org/10.1016/j.meatsci.2019.05.009

Kamruzzaman M, Makino Y, Oshita S (2016) Online monitoring of red meat colour using hyperspectral imaging. Meat Sci 116:110–117. https://doi.org/10.1016/j.meatsci.2016.02.004

Krzywicke (1982) The determination of haem pigments in meat. Meat Sci 7(1):29–36. https://doi.org/10.1016/0309-1740(82)90095-X

Karoui R, Mouazen AM, Dufour E, Pillonel L, Schaller E, Baerdemaeker JD, Bosset JO (2006) Chemical characterisation of European Emmental cheeses by near infrared spectroscopy using chemometric tools. Int Dairy J 16(10):1211–1217. https://doi.org/10.1016/j.idairyj.2005.10.002

Kamruzzaman M, ElMasry G, Sun DW, Allen P (2012) Prediction of some quality attributes of lamb meat using near-infrared hyperspectral imaging and multivariate analysis. Anal Chim Acta 714:57–67. https://doi.org/10.1016/j.aca.2011.11.037

Lorente D, Aleixos N, Gomez-Sanchis J, Cubero S, Garcia-Navarrete OL, Blasco J (2012) Recent advances and applications of hyperspectral imaging forfruit and vegetable quality assessment. Food Bioprocess Technol 5(4):1121–1142. https://doi.org/10.1007/s11947-011-0725-1

Lohumi S, Lee S, Lee H, Kim MS, Lee WH, Cho BK (2016) Application of hyperspectral imaging for characterization of intramuscular fat distribution in beef. Infrared Phys Technol 74:1–10. https://doi.org/10.1016/j.infrared.2015.11.004

Liu Y, Cao XD, Meng XL, Wu T, Yan XZ, Luo QH (2019) Impact of class noise on performance of hyperspectral band selection based on neighborhood rough set theory. Chemom Intell Lab Syst 188:37–45. https://doi.org/10.1016/j.chemolab.2019.03.003

Mancini RA, Hunt MC (2005) Current research in meat color. Meat Sci 71(1):100–121. https://doi.org/10.1016/j.meatsci.2005.03.003

Mancini RA, Ramanathan R 2020 Molecular basis of meat color, In: Ashim KB, Prabhat KM (Eds) In Meat Quality Analysis, Academic Press, pp 117–129. https://doi.org/10.1016/B978-0-12-819233-7.00008-2

Mancini R 2013 Meat Color. In: Kerth CR (Ed), The science of meat quality, Wiley, Oxford, UK, pp 177–198. https://doi.org/10.1002/9781118530726.ch9

Ma J, Sun DW (2020) Prediction of monounsaturated and polyunsaturated fatty acids of various processed pork meats using improved hyperspectral imaging technique. Food Chem 321:126695. https://doi.org/10.1016/j.foodchem.2020.126695

Ma J, Sun DW, Pu HB, Wei QY, Wang XM (2019) Protein content evaluation of processed pork meats based on a novelsingle shot (snapshot) hyperspectral imaging sensor. J Food Eng 240:207–213. https://doi.org/10.1016/j.jfoodeng.2018.07.032

Maria FF, Luis G (2014) Consumer preference, behavior and perception about meat and meat products: An overview. Meat Sci 98:361–371. https://doi.org/10.1016/j.meatsci.2014.06.025

Mo LN, Chen HZ, Chen WH, Feng QX, Xu LL (2020) Study on evolution methods for the optimization of machine learning models based on FT-NIR spectroscopy. Infrared Phys Technol 108:103366. https://doi.org/10.1016/j.infrared.2020.103366

Nguyen T, Nguyen KP, Lee JB, Kim JG (2016) Met-myoglobin formation, accumulation, degradation, and myoglobin oxygenation monitoring based on multiwavelength attenuance measurement in porcine meat. J Biomed Opt 21(5):57002. https://doi.org/10.1117/1.JBO.21.5.057002

Nguyen T, Kim S, Kim JG (2019) Diffuse reflectance spectroscopy to quantify the met-myoglobin proportion and meat oxygenation inside of pork and beef. Food Chem 275:369–376. https://doi.org/10.1016/j.foodchem.2018.09.121

Osborne BG 2000 Near-infrared spectroscopy in food analysis. Encyclopedia of Analytical Chemistry. https://doi.org/10.1002/9780470027318.a1018

Pu H, Kamruzzaman M, Sun DW (2015) Selection of feature wavelengths for developing multispectral imaging systems for quality, safety and authenticity of muscle foods-a review. Trends Food Sci Technol 45:86–104. https://doi.org/10.1016/j.tifs.2015.05.006

Qin JW, Chao K, Kim MS, Lu RF, Burks TF (2013) Hyperspectral and multispectral imaging for evaluating food safety and quality. J Food Eng 118:157–171. https://doi.org/10.1016/j.jfoodeng.2013.04.001

Shin S, Lee Y, Kim S, Choi S, Kim JG, Lee K (2021) Rapid and nondestructive spectroscopic method for classifying beef freshness using a deep spectral network fused with myoglobin information. Food Chem 352:129329. https://doi.org/10.1016/j.foodchem.2021.129329

Shao YY, Wang KL, Xuan GT, Gao C, Hu ZH (2021) Soluble solids content monitoring for shelf-life assessment of table grapes coated with chitosan using hyperspectral imaging. Infrared Phys Technol 115:103725. https://doi.org/10.1016/j.infrared.2021.103725

Tao FF, Peng YK (2015) A nondestructive method for prediction of total viable count in pork meat by hyperspectral scattering imaging. Food Bioprocess Technol 8(1):17–33. https://doi.org/10.1007/s11947-014-1374-y

Vaiphasa C (2006) Consideration of smoothing techniques for hyperspectral remote sensing. ISPRS J Photogramm Remote Sens 60(2):91–99. https://doi.org/10.1016/j.isprsjprs.2005.11.002

Wang C, Wang S, He X, Wu L, Li Y, Guo J (2020) Combination of spectra and texture data of hyperspectral imaging for prediction and visualization of palmitic acid and oleic acid contents in lamb meat. Meat Sci 169:108194. https://doi.org/10.1016/j.meatsci.2020.108194

Wang YJ, Li TH, Li LQ, Ning JM, Zhang ZZ (2020) Evaluating taste-related attributes of black tea by micro-NIRS. J Food Eng 290:110181. https://doi.org/10.1016/j.jfoodeng.2020.110181

Wan GL, Liu GS, He JG, Luo RM, Cheng LJ, Ma C (2020) Feature wavelength selection and model development for rapid determination of myoglobin content in nitrite-cured mutton using hyperspectral imaging. J Food Eng 287:110090. https://doi.org/10.1016/j.jfoodeng.2020.110090

Wei X, He JC, Zheng SH, Ye DP (2020) Modeling for SSC and firmness detection of persimmon based on NIR hyperspectral imaging by sample partitioning and variables selection. Infrared Phys Technol 105:103099. https://doi.org/10.1016/j.infrared.2019.103099

Weng SZ, Guo BQ, Tang PP, Yin X, Pan FF, Zhao JL, Huang LS, Zhang DY (2020) Rapid detection of adulteration of minced beef using Vis/NIR reflectance spectroscopy with multivariate methods. Spectrochimica Acta-Part A Mol Biomol Spectros 230:118005. https://doi.org/10.1016/j.saa.2019.118005

Wu JH, Peng YK, Li YY, Wang W, Chen JJ, Dhakal S (2012) Prediction of beef quality attributes using VIS/NIR hyperspectral scattering imaging technique. J Food Eng 109(2):267–273. https://doi.org/10.1016/j.jfoodeng.2011.10.004

Wu D, Shi H, He Y, Yu XJ, Bao YD (2013) Potential of hyperspectral imaging and multivariate analysis for rapid and non-invasive detection of gelatin adulteration in prawn. J Food Eng 119:680–686. https://doi.org/10.1016/j.jfoodeng.2013.06.039

Xu YF, Zhang HJ, Zhang C, Wu P, Li JB, Xia Y, Fan SX (2019) Rapid prediction and visualization of moisture content in single cucumber (Cucumis sativus L.) seed using hyperspectral imaging technology. Infrared Physics & Technology 102: 103034. https://doi.org/10.1016/j.infrared.2019.103034

Yu JY, Liu GS, Zhang JJ, Zhang C, Fan NY, Xu YQ, Guo JJ, Yuan JT (2021) Correlation among serum biochemical indices and slaughter traits, texture characteristics and water-holding capacity of Tan sheep. Ital J Anim Sci 20(1):1781–1790. https://doi.org/10.1080/1828051X.2021.1943014

Yu HD, Qing LW, Yan DT, Xia GH, Zhang CH, Yun YH, Zhang WM (2021) Hyperspectral imaging in combination with data fusion for rapid evaluation of tilapia fillet freshness. Food Chem 348:129129. https://doi.org/10.1016/j.foodchem.2021.129129

Yang XY, Liu GS, He JG, Kang NB, Yuan RR, Fan NY (2021) Determination of sugar contents in jujube by NIR-hyperspectral imaging coupled with chemometric analysis. J Food Sci 86(4):1201–1214. https://doi.org/10.1111/1750-3841.15674

Yuan RR, Liu GS, He JG, Ma C, Cheng LJ, Fan NY, Ban JJ, Li Y, Sun YR (2020) Determination of metmyoglobin in cooked tan mutton using Vis/NIR hyperspectral imaging system. J Food Sci 85(5):1403–1410. https://doi.org/10.1111/1750-3841.15137

Yuan RR, Liu GS, He JG, Wan GL, Fan NY, Li Y, Sun YR (2021) Classification of Lingwu long jujube internal bruise over time based on visible near-infrared hyperspectral imaging combined with partial least squares-discriminant analysis. Comput Electron Agric 182:106043. https://doi.org/10.1016/j.compag.2021.106043

Yun YH, Bin H, Liu DL, Xu L, Yan TL, Cao DS, Xu QS (2019) A hybrid variable selection strategy based on continuous shrinkage of variable space in multivariate calibration. Anal Chim Acta 1058:58–69. https://doi.org/10.1016/j.aca.2019.01.022

Zhang N, Liu X, Jin XD, Li C, Wu X, Yang SQ, Ning JF, Paul Y (2017) Determination of total iron-reactive phenolics, anthocyanins and tannins in wine grapes of skins and seeds based on near-infrared hyperspectral imaging. Food Chem 237:811–817. https://doi.org/10.1016/j.foodchem.2017.06.007

Publisher's Note Springer Nature remains neutral with regard to jurisdictional claims in published maps and institutional affiliations.